Multi-scale parameterization of neural rhythmicity with lagged Hilbert autocoherence

Siqi Zhang[1,2], Maciej J Szul[1,2], Sotirios Papadopoulos[1,2,3], Alice Massera[1,2], Holly Rayson[1,2*], James J Bonaiuto[1,2*]

1) Marc Jeannerod Institute of Cognitive Sciences, ISC, CNRS UMR5229, Lyon, France

2) Université Claude Bernard Lyon 1, Université de Lyon, France

3) Lyon Neuroscience Research Center, CRNL, INSERM U1028, CNRS UMR5292, Lyon, France

* authors contributed equally

Corresponding author: Holly Rayson

Keywords: lagged coherence, rhythmicity, oscillations, bursts, periodic activity, spectral parameterization

Abstract

Analysis of neural activity in different frequency bands is ubiquitous in systems and cognitive neuroscience. Recent analytical breakthroughs and theoretical developments rely on phase maintenance of oscillatory signals without considering whether or not this assumption is met. Lagged (auto)coherence, the coherence between a signal and itself at increasing temporal delays, has been proposed as a way to quantify the rhythmicity, or periodicity, of a signal. However, current Fourier-based lagged autocoherence algorithms suffer from poor spectral accuracy and resolution, aliasing effects that become more pronounced at higher frequencies, and conflation with amplitude covariation, especially in frequency ranges in which the signal power is low. We introduce a continuous lagged autocoherence metric, lagged Hilbert autocoherence, that addresses these shortcomings by using multiplication in the frequency domain for precise bandpass filtering, instantaneous analytic signals via the Hilbert transform, and thresholding using the amplitude covariation of surrogate data generated by an autoregressive model. We show that this version of lagged coherence yields vastly higher spectral accuracy and resolution than lagged Fourier autocoherence, and that this unlocks additional, increasingly fine-grained applications. This includes examination of: 1) frequency-specific differences in rhythmicity between conditions, 2) changes in signal rhythmicity during learning, and 3) the relationship between frequency-specific rhythmicity and behavior, trial-by-trial. Lagged Hilbert autocoherence thus offers a significant toolset advancement for analysis of neurophysiological rhythmicity.

1. Introduction

Neural oscillations are ubiquitous in the study of cognitive and systems neuroscience. The rhythmic activity of neuronal populations, spanning various frequency bands, forms a fundamental mechanism in the orchestration of large-scale brain network dynamics, influencing a multitude of cognitive and behavioral functions (Buzsáki and Freeman, 2015). Consequently, the accurate and reliable analysis of these oscillatory signals is paramount for advancing our understanding of brain function. The majority of theoretical developments to date have assumed the phase maintenance of oscillatory signals (Bonnefond et al., 2017; Fries, 2015; Jensen et al., 2015), however the veracity of this assumption is often overlooked in practice (Donoghue et al., 2022).

In response to this challenge, we introduce a novel metric - lagged Hilbert autocoherence (LHaC) - that allows for several new types of neurophysiological analysis. The concept of lagged coherence, which captures the coherence of a signal with itself over increasing temporal delays, has been advanced as an effective method to measure the rhythmicity or periodicity of a signal (Fransen et al., 2016, 2015). While having yielded important insights into the underlying nature of alpha and beta power, existing lagged coherence algorithms based on the Fourier transform possess a number of critical limitations. These include poor spectral accuracy and resolution, aliasing effects at higher frequencies, and conflation of coherence with amplitude covariation in frequency ranges with lower signal power. Lagged Hilbert autocoherence significantly addresses the above limitations by employing multiplication in the frequency domain to achieve precise bandpass filtering, instantaneous analytic signals via the Hilbert transform, and a thresholding

method using the amplitude covariation of surrogate data generated by an autoregressive model. This paper demonstrates the algorithm's superior spectral accuracy and resolution over lagged Fourier autocoherence (LFaC). Here, we showcase the utility of lagged Hilbert autocoherence by comparing the association between frequency-specific rhythmicity and behavior, first in simulation, and then in EEG, MEG, and LFP data from humans and non-human primates. We demonstrate its ability to identify between epoch and condition differences in rhythmicity, changes in rhythmicity with sensorimotor learning over trial blocks, and trial-by-trial associations between rhythmicity and behavior.

2. Methods

2.1 Lagged autocoherence algorithm

The original lagged coherence algorithm (Fransen et al., 2015) is based on a coherence metric commonly used to evaluate functional connectivity. Whereas coherence is typically applied to two different signals, lagged coherence operates on a single signal and a lagged copy of itself. We therefore refer to it as lagged *auto*-coherence. The algorithm breaks the signal into epochs, applies a Fourier transform to each epoch, and subsequently calculates coherence between temporally separated epochs at a given frequency. The temporal gap between each epoch is specified in terms of cycles corresponding to the target frequency. The duration of each epoch can be set to match a prescribed number of cycles (e.g. 3 cycles no matter what the evaluated lag; Fransen et al., 2016, 2015; Little et al., 2019; Muralidharan et al., 2023), or to the evaluated lag (Rayson et al., 2022; Szul et al., 2023), and the epochs can be either overlapping (Little et al., 2019; Rayson et al., 2022; Szul et al., 2023), or non-overlapping (Fransen et al., 2016, 2015; Muralidharan et al., 2023). Lagged autocoherence (λ) for a frequency f, is defined by:

$$\lambda(f) = \left| \frac{\sum_{n=1}^{N-1} A_n(f) A_{n+1}(f) e^{j(\phi_n(f) - \phi_{n+1}(f))}}{\sqrt{\left(\sum_{n=1}^{N-1} A_n(f)^2\right)\left(\sum_{n=1}^{N-1} A_{n+1}(f)^2\right)}} \right| \quad [1\text{-}1]$$

where $A_n(f)e^{j\phi_n(f)}$ is the expression of the complex-valued Fourier coefficient of epoch n for frequency f, with amplitude A and phase φ. The Fourier coefficients are obtained by applying a Fourier transform to a Hann-tapered signal. The numerator, when divided by the number of epoch pairs, is called the lagged autospectrum. The lagged autospectrum depends on the difference in phase between epoch pairs, but also on their amplitudes, and therefore it is normalized by the product of the sum of amplitudes from the first and second epoch of each pair, resulting in a metric bounded by 0 and 1. Lagged Fourier autocoherence (LFaC) thus serves as a measure of phase synchrony between lagged segments of the signal at a specific frequency.

2.2 Lagged Hilbert autocoherence algorithm

Lagged Hilbert autocoherence (LHaC) diverges from the previously described lagged autocoherence algorithm by using Hilbert coherence (Bruña et al., 2018; Hu and Liang, 2012), and is therefore an adaptation of lagged Hilbert coherence (Pascual-Marqui et al., 2024). LHaC generates a continuous analytic signal using the Hilbert transform and then calculates coherence at a series of single time points corresponding to a specific lag duration. To compute LHaC at a

given frequency and lag (in cycles of that frequency), the signal is first zero-padded and then bandpass-filtered by multiplication with a Gaussian kernel in the frequency domain (Figure 1a). The Gaussian is centered on the target frequency, and the kernel width (which is representative of the spectral width of the filter) can be appropriately adjusted. For single frequency analysis, we utilize a kernel width of 1Hz. However, for a set of evenly spaced frequencies, the width is determined by the frequency resolution of the set. The resulting product is a bandpass filtered version of the signal. The Hilbert transform is subsequently applied to the bandpass filtered signal to yield the instantaneous amplitude, $A_t(f)$, and phase, $\phi_t(f)$, of the signal at the specified frequency, *f*, for each time point, *t*. Following this, for a given signal recorded at a sampling rate *Fs*, lagged autocoherence is computed at time point pairs, starting from time point *s*, and separated in time by a delay, *d* (by time points), per the specified lag, *l*, and frequency ($d = \frac{l}{f} * Fs$):

$$\lambda_s(f,l) = \left| \frac{\sum_{t=0}^{T/d-1} A_{s+td}(f) A_{s+(t+1)d}(f) e^{j\left(\phi_{s+td}(f) - \phi_{s+(t+1)d}(f)\right)}}{\sqrt{\left(\sum_{t=0}^{T/d-1} A_{s+td}(f)^2\right)\left(\sum_{t=0}^{T/d-1} A_{s+(t+1)d}(f)^2\right)}} \right| \quad [1\text{-}2]$$

where *T* is the total number of time points. The starting time point, *s*, is initialized to the first time point in the series and is then shifted by one until all time points are incorporated (until *s* = *d* - 1), and the resulting lagged autocoherence values are averaged over all shifts (Figure 1b):

$$\lambda(f,l) = \sum_{s=1}^{d-1} \frac{\lambda_s(f,l)}{d-1} \quad [1\text{-}3]$$

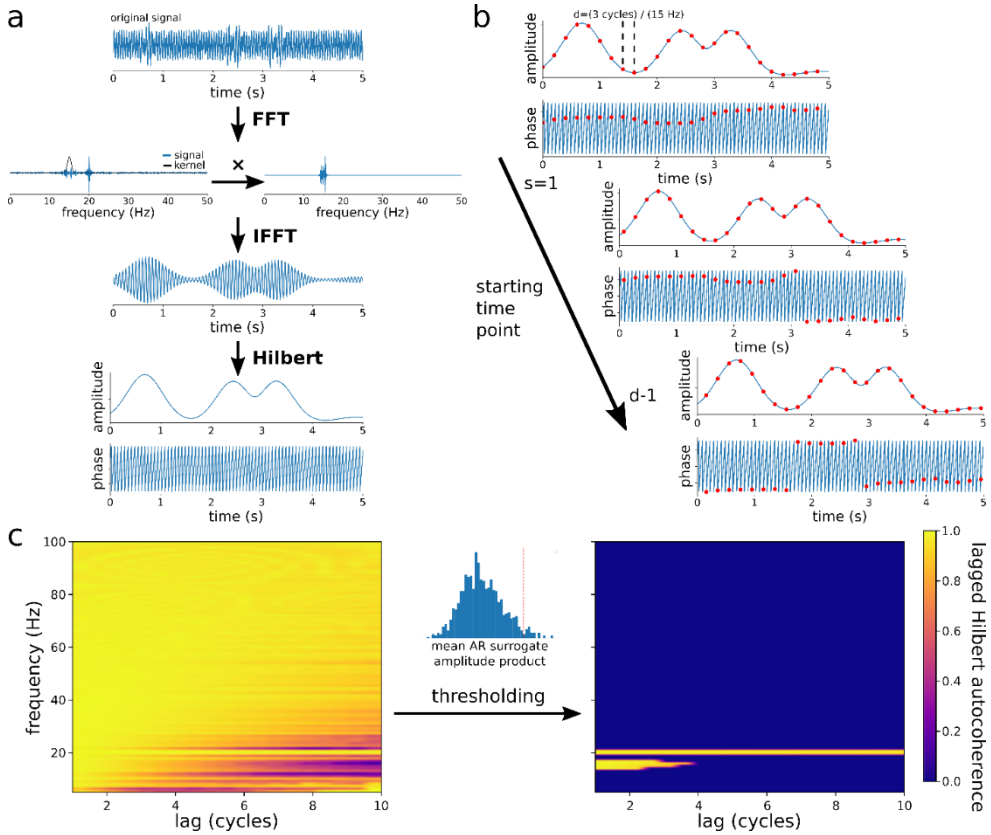

Figure 1. The lagged Hilbert autocoherence algorithm. a) The original time series is bandpass filtered at a given frequency using multiplication by a narrow Gaussian kernel in the frequency domain (centered around 15 Hz in this

example) in order to obtain precise filtering), and then the Hilbert transform is used to obtain the instantaneous amplitude envelope and phase. b) Lagged autocoherence is computed using the instantaneous amplitude and phase between time steps separated by a given lag (evaluated at 15 Hz and 3 lag cycles in this example: d = (3 cycles / 15 Hz) × Fs = 200 time points), and averaged over incremental shifts of the starting time point (as illustrated in equations [1-2] [1-3]). c) Lagged autocoherence is evaluated at a range of lags and frequencies. A threshold is computed from the average broadband amplitude product between time points of AR model-generated surrogate data. Lagged Hilbert autocoherence is set to zero wherever the denominator is less than this threshold.

This approach should theoretically result in a spectrally and temporally resolved measure of lagged autocoherence, however amplitude correlations can be introduced by bandpass filtering in a frequency range in which the signal has low power. In equation [1-2], this situation results in a very low value for the numerator, but also a very low value for the denominator, resulting in a lagged autocoherence value of nearly 1. Problems related to amplitude correlation across sites (Cohen and Tsuchiya, 2018; Srinath and Ray, 2014) and low-frequency noise (Miles, 2011) have been previously identified with the standard coherence metric, and it has been suggested to use a coherence threshold of the lowest measurable value for two independent signals (Carter, 1977; Gallet and Julien, 2011; Miles, 2011). Such thresholds are typically based on surrogate data generated by white noise (Le Van Quyen et al., 2001) or Gaussian processes (Miles, 2011), or by shuffling the data (Lachaux et al., 2000). Based on suggestions for generating surrogate data to test for the presence of periodic activity (Brookshire, 2022), we use a parametric bootstrap method based on autoregressive (AR) models which preserve the aperiodic temporal structure of the signal, but destroy the periodic structure (Mann and Lees, 1996). The signal is first band-pass filtered in the range of frequencies that LHC is being evaluated within, and an autoregressive model with one positive coefficient (AR(1)) is fit to the filtered data. A large sample of surrogate signals is then generated from the model (n = 1000), and from each of them, the mean broadband amplitude product between successive time points is computed:

$$Ap_{mean} = \sum_{t=0}^{T-1} \frac{A_t A_{t+1}}{T-1}$$

The 95th percentile of Ap_{mean} over all surrogate signals is then used as a threshold for LHaC. If the denominator of equation [1-2] is less than this threshold, LHaC is set to 0 (Figure 1c). This procedure is applied for each trial independently.

Implementations of both LFaC and LHaC in MATLAB and python, demos, and code for all simulations and analyses can be found at https://github.com/danclab/lagged_hilbert_autocoherence.

2.3 Simulations

In order to compare the spectral accuracy and precision of LFaC and LHaC, we generated sinusoidal signals ranging from 10 to 50 Hz in increments of 5 Hz. For each frequency, 100 simulated trials were generated with a random initial phase for each trial. Trials had a duration of 5 s and a sampling rate of 1 kHz. The amplitude of the sinusoidal signals varied from -1 to 1 (au). To incorporate a realistic noise component, pink noise with a slope of 1 was introduced, scaled to achieve an SNR of 0 dB. PSDs for each trial were computed using Welch's method (Welch, 1967), with a 1 s window and 50% overlap. Lagged Fourier and Hilbert autocoherence were then

computed across a range of 5 to 100 Hz, in 0.5 Hz increments, and from 1 to 6 cycles, in 0.5-cycle increments. The RMSE was computed between normalized PSDs and lagged autocoherence (averaged over lag cycles). Frequency spread was computed as the standard deviation of lagged autocoherence (averaged over lag cycles) over frequencies. For each simulated oscillation frequency, the RMSEs and frequency spreads of LFaC and LHaC were compared using Wilcoxon signed-rank tests (Bonferroni-corrected).

To determine the sensitivity of LHaC to burst duration and the number of bursts, we ran two sets of simulations, each with 100 simulated trials of 6 s with a 1 kHz sampling rate and an SNR of 0 dB. Both sets of simulations involved generating signals with bursts of oscillatory activity at frequencies ranging from 20 to 50 Hz, in increments of 5 Hz. The first set of simulations generated one burst per trial, with a random duration from 2 to 5 cycles in each trial. In the second set of simulations, there were 1 to 5 bursts in each trial, each 3 cycles long. In both sets of simulations, LHaC was evaluated from 5 to 100 Hz in 0.5 Hz increments, and from 1 to 20 cycles, in increments of 0.5 cycles. The decrease in LHaC with increasing lags was then evaluated by fitting an inverse sigmoid function to the LHaC at the simulated burst frequency over all evaluated lag cycles:

$$y(l) = 1 - \frac{1}{1 + e^{-k(l - l_0)}}$$

where l is the evaluated lag cycle, and the fitted variables k and l_0 determine the rate of LHaC decay with increasing lags, and the crossover point in terms of lag cycles corresponding to the greatest lagged autocoherence decrease, respectively. Linear models were used to evaluate the relationship between the fitted values of k and l_0 and the simulated burst duration or number. Each of these models had k or l_0 as the dependent variable, and frequency, a single burst metric, and their interaction as fixed effects. The burst metrics used were burst duration in seconds, burst duration in cycles, and the number of bursts. Fixed effects were assessed using type III F tests (car v3.1.0; Fox et al., 2019), and for each inverse sigmoid parameter, models with burst duration in seconds or cycles were compared using the Akaike information criterion (AIC; Akaike, 1974, 1973).

2.4 Datasets and Applications

After establishing the utility of lagged Hilbert autocoherence and contrasting it with lagged Fourier autocoherence in simulation, we applied the new algorithm to several different empirical datasets in order to investigate the practical value of our new method.

2.4.1 EEG data

EEG data were previously recorded from human infants and adults as part of a study investigating the neural bases of action execution and observation (methodological details can be found in Cannon et al., 2014; Yoo et al., 2016). The experiment was approved by the University of Maryland Institutional Review Board, with informed consent obtained from the infants' parents and adult participants. After exclusions, the final sample included 28 9-month-old infants, 33 12-month-old infants, and 22 adults. Infant and adult participants performed the same reach-and-grasp task. Infants were seated on their caregiver's lap and adults in a chair during an observation and execution condition. In the observation trials, participants watched a female presenter interact

with a toy using a hand-operated tool, while in the execution trials, participants were given the opportunity to reach for the toy themselves. EEG data were recorded using a 65-channel HydroCel Geodesic Sensor Net (Electrical Geodesics, Inc., Eugene, OR), sampled at 500 Hz, with the vertex (Cz) electrode used as an online reference, and impedances kept below 100 kΩ. The EEG data were later exported to a MATLAB compatible format for offline processing.

Data preprocessing was conducted in MATLAB R2018a, using a modified MADE pipeline (Debnath et al., 2020) with artifact detection routines from the NEAR pipeline (Kumaravel et al., 2022). Signals were high-pass filtered at 1 Hz and low-pass filtered at 100 Hz. Artifact-laden channels were identified and removed with the NEAR pipeline's local outlier factor metric, followed by artifact subspace reconstruction for non-stereotyped artifacts. Independent component analysis (ICA) was performed on 1s epochs to detect and remove stereotyped artifacts like eye blinks, with artifactual components identified via the Adjusted-ADJUST plugin (Leach et al., 2020; Mognon et al., 2011). Behavioral events were captured via video recording, and for both conditions, five coded time points were used to segment the EEG time series into 3.5s epochs centered on the baseline period, the go cue, the first touch with the hand, the completion of the grasp, and the end of the movement. Epochs exceeding 10% artefacted channels were excluded; otherwise, artefacted channels were interpolated. Missing channels were subsequently interpolated, data were average re-referenced, and line noise (60 Hz) was removed using the Zapline algorithm (de Cheveigné, 2020).

Lagged Hilbert autocoherence was computed for each participant in both the observation and execution conditions, and in each epoch, from 4 to 100Hz in 0.5 Hz increments and 0.1-4.5 cycles in increments of 0.05 cycles. The lagged coherence values were averaged over all electrodes in C3 and C4 clusters (E16, E20, E21, E22, E41, E49, E50, E51). To explore the interacting effects of condition and epoch on LHaC, we applied a mass-univariate two-way repeated measures ANOVA (2 conditions by 5 epoch levels; including the baseline epoch) within each age group, and follow-up mass-univariate t-tests to explore significant interactions between condition and epoch. All of these analyses were corrected for multiple comparisons at the cluster level.

2.4.2 MEG data

High precision MEG data were recorded for a previous experiment from 38 human adults (25 female) as they performed a visually cued button press task (methodological details can be found in the corresponding manuscript; Szul et al., 2023). The study protocol was in accordance with the Declaration of Helsinki, and all participants gave written informed consent which was approved by the regional ethics committee for human research (CPP Est IV - 2019-A01604–53). The data were recorded using a 275-channel Canadian Thin Films (CTF) MEG system featuring SQUID-based axial gradiometers (CTF MEG Neuro Innovations, Inc. Coquitlam, Canada) inside a magnetically shielded room. Visual stimuli were displayed via a projector on a screen roughly 80 cm from the participant, and a joystick (NATA Technologies, Canada) was used for participant responses. The MEG data collected were digitized continuously at a sampling rate of 1200 Hz. Participants performed a cued visuomotor adaptation task, making rapid joystick-based movements to reach visually presented targets, guided by a random dot kinematogram (RDK). In some trials, the position of the cursor indicating the joystick position was rotated by 30°.

Participants were divided into two groups, explicit (N = 20) and implicit (N = 18). The direction of the explicit group's visuomotor rotation was predicted by the RDK's direction of coherent motion, while the reaches of the implicit group were subject to a constant rotation unrelated to the RDK. Participants underwent training blocks, followed by one block of trials without visuomotor rotation, seven blocks of trials with visuomotor rotation, and a final washout block without rotation. The MEG data was preprocessed using the MNE-Python toolbox (Gramfort et al., 2014), downsampled to 600 Hz, and filtered with a low pass 120 Hz zero-phase FIR filter. Line noise was removed using an iterative version of the Zapline algorithm (de Cheveigné, 2020). Ocular and cardiac artifacts were identified and removed using Independent Component Analysis, correlating components with eye movement signals and ECG R peak detection, respectively.

The data was then epoched around the visual stimulus onset (-1 to 2 s) and the end of the reaching movement (-1 to 1.5 s), focusing on 11 sensors above the left sensorimotor area. One subject from the explicit group was excluded from further analysis due to a technical error during recording (final implicit N = 19, explicit N = 18). Lagged Hilbert autocoherence was computed for each epoch of each trial from 5 to 100 Hz in increments of 0.5 Hz and from 1 to 4 lag cycles in increments of 0.1 cycles. For each subject, lagged autocoherence values were then averaged over channels and then over trials within each block and normalized according to the maximal lagged autocoherence in the first block. Within the alpha (7 - 13 Hz) and beta (15 - 30 Hz) bands, the total lagged autocoherence and lagged coherence at a specific lag (3 cycles for alpha and 1 cycle for beta based on the lag cycles with the maximal variability across subjects and blocks) were computed for each block of trials, relative to the first block. For each block, these values were compared between groups using a bootstrap permutation test. This involved generating null distributions (N = 10,000) by sampling participants with replacement and randomly assigning them to a group before computing the group difference.

2.4.3 LFP data

LFP data used in this study for analysis came from two adult male rhesus monkeys (Macaca mulatta), collected for an earlier reported experiment (methodological details can be found in the corresponding manuscript; Dixon et al., 2021). The study complied with guidelines from the US National Institutes of Health and the University of California, Berkeley Animal Care and Use Committee. Neuronal responses were recorded bilaterally from the dorsal premotor and primary motor cortices via 24–32 channel multi-site probes, with 15 µm electrode contacts spaced by 100 µm along a single shank. Local field potentials were recorded at a 1 kHz sampling rate. The monkeys were trained to perform a three-phase instructed-delay reaching task in 3-D space, following visual cues and variable intervals, and monitored with optical motion tracking.

The data were epoched from 500 ms before the go signal, to 500 ms afterwards. Spectral densities were computed separately for each contact from 10 to 100 Hz using Welch's method (Welch, 1967) with a 1 s window, 50% overlap, and double padding, resulting in a frequency resolution of 0.33 Hz. Relative power spectra were computed by, for each frequency, normalizing the power in each channel by dividing it by the maximum power over all channels at that frequency (Mendoza-Halliday et al., 2024). Because relative beta power was strongest in the deepest electrode contact in every session (Figure S1), lagged Hilbert autocoherence was computed on

signals from this contact from 10 Hz to 100 Hz in increments of 1 Hz, and 0.5 to 2.5 cycles in increments of 0.1. The frequency range of the beta band was determined according to the full width at half maximum (FWHM) around the peak LHaC within the beta band (evaluated at 0.5 cycles). LHaC was then averaged within the beta frequency range, resulting in beta-specific LHaC as a function of lag cycles. The sum of beta LHaC values over all evaluated lagged cycles (referred to below as 'total LHaC') was then related to the trial-by-trial behavior.

In each trial, response time (RT) was measured as the time elapsed between the go cue and the start of the movement. We then tested the predictiveness of total beta LHaC for RT in different time windows relative to the go cue (1s windows starting from 1s, 0.75s, 0.5s, 0.25s, and 0s prior to the go cue). Linear mixed models were used to examine the effects of hemisphere, LHaC, and their interaction on RT in each time window.

3. Results

3.1 Simulation comparison of lagged Fourier autocoherence and lagged Hilbert autocoherence

We first set out to determine, in simulation, the spectral accuracy and precision of LHaC, as well as its dependence on burst duration or number of bursts. We compared lagged Fourier autocoherence and lagged Hilbert autocoherence by simulating oscillatory neural signals at frequencies from 10 to 50 Hz. In order to assess spectral accuracy and precision, we averaged each lagged coherence metric over simulated trials and then over 1 to 6 lag cycles. We then computed the RMSE between normalized PSDs of the simulated signal and lagged autocoherence, and the frequency spread (standard deviation over frequencies) of lagged autocoherence. The RMSE provides an index of how closely each lagged autocoherence measure reproduces the spectral power profile. Lower RMSE indicates higher accuracy in identifying the underlying frequency-specific rhythmicity. The frequency spread indicates the precision of the lagged autocoherence measure over frequencies, with lower values reflecting a sharper and more precise spectral profile. Across simulations, we found the Hilbert-based lagged autocoherence demonstrated significantly higher spectral accuracy compared to LFaC, with lower RMSE relative to the PSD of the simulated signal for each simulated frequency (Figure 2a-d; all Z = -8.68, p < 0.001). Lagged Hilbert autocoherence also had greater precision, with lower frequency spread than LFaC for each simulated frequency (Figure 2a-c,e; all Z = -8.68, p < 0.001). Given the significant advantage of LHaC in terms of spectral accuracy and precision compared to LFaC, we focused the subsequent simulations and analyses on LHaC.

Having established that LHaC has higher spectral accuracy and precision than LFaC, we then set out to determine how the number and duration of bursts of activity affect this metric over increasing lag cycles. We therefore simulated bursts of oscillatory activity, spanning frequencies of 20 to 50 Hz. In the first simulation set, each trial was characterized by a single burst whose duration was uniformly randomized between 2 and 5 cycles. Conversely, in the subsequent set, every burst lasted for 3 cycles, but each trial consisted of 1 to 5 bursts (with a uniform random distribution over trials). We fit an inverse sigmoid function to LHaC at the simulated frequency, yielding both a crossover point (Figure 2f, inset) and a decay rate (Figure 2i, inset), representing

the number of lag cycles corresponding to the maximal decrease in lagged coherence and the rate of this decrease, respectively. The fitted values for both the crossover point and decay rate were then compared against the burst duration and the number of bursts for every simulated frequency. This revealed a linear relationship between the inverse sigmoid crossover point and burst duration, as measured in both absolute duration (seconds; $F(1) = 18.70$, $p < 0.001$) and frequency cycle counts ($F(1) = 598.73$, $p < 0.001$). However, the relationship exhibited frequency-dependent variations in offset when quantified in seconds (Figure 2f), yet was consistent across frequencies when measured in cycles (Figure 2g), resulting in a better model fit for the model with burst duration expressed in cycles (ΔAIC = -1,120.24). In a contrasting pattern, the decay rate of the inverse sigmoid had an inverse relationship with burst duration (seconds: $F(1) = 506.27$, $p < 0.001$; cycles: $F(1) = 65.74$, $p < 0.001$). However, here the offset of the relationship varied with frequency when assessed in cycle counts (Figure 2j) but remained invariant in terms of absolute burst duration (Figure 2i), resulting in a better model fit for the model with burst duration expressed in seconds (ΔAIC = -953.26). Notably, the frequency of bursts had no effect on either the crossover point (Figure 2h; $F(1) = 0.02$, $p = 0.891$) or decay rate (Figure 2k; $F(1) = 0.30$, $p = 0.582$) of the inverse sigmoid, regardless of the frequency. LHaC therefore offers an accurate and reliable metric of burst duration, irrespective of burst rate.

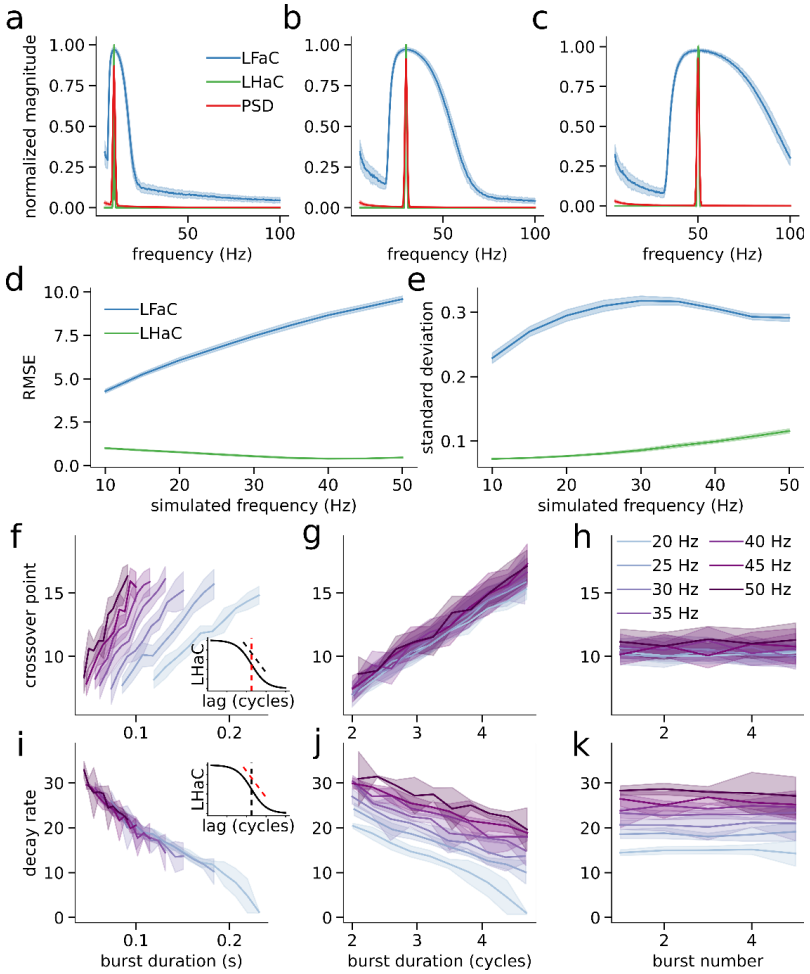

Figure 2. Lagged Fourier autocoherence and lagged Hilbert autocoherence simulation results. Lagged Fourier autocoherence and lagged Hilbert autocoherence averaged over 1 to 6 cycles and normalized, compared to the normalized PSD for simulations of oscillations at 10 (a), 25 (b), and 50 Hz (c). d) RMSE of the averaged and normalized

LFaC and LHaC metrics compared to the normalized PSD over simulated oscillations from 10 to 50Hz. e) As in (d), for the standard deviation over frequencies of LFaC and LHaC, averaged over 1 to 6 cycles. f) For each simulated burst frequency, the fitted crossover point of the inverse sigmoid (inset: red dashed line) as a function of burst duration in seconds. The solid lines denote the mean within 10 equally spaced bins, and the shaded area represents the standard deviation. g) As in (f), with burst duration expressed in terms of the number of cycles of the simulated burst frequency. h) As in (f), for the number of simulated bursts. i) For each simulated burst frequency, the decay rate of the inverse sigmoid (inset: red dashed line) as a function of burst duration in seconds. The solid lines denote the mean within 10 equally spaced bins, and the shaded area represents the standard deviation. j) As in (i), with burst duration expressed in cycles. k) As in (i), for the number of simulated bursts.

3.2 Sensorimotor rhythmicity is differentially modulated during action observation and execution conditions

Following the validation of the spectral accuracy and precision of lagged Hilbert autocoherence for assessing signal rhythmicity, we aimed to demonstrate its utility for assessing group-level differences in neural activity rhythmicity across experimental conditions and task epochs. LHaC was applied to EEG signals recorded over sensorimotor cortex in 9- and 12-month-old infants and adults during both execution and observation of grasping a toy (Cannon et al., 2014; Yoo et al., 2016). The within-group averaged LHaC across conditions and epochs of 9-month (Figure 3a), 12-month (Figure 3b), and adult group (Figure 3c) exhibited peak values within the theta, alpha, beta, and gamma frequency ranges at low lags, which increased in frequency between infancy and adulthood. In the two infant groups, the peak in the alpha frequency range was similar in frequency (~8 Hz), but differed in terms of decay rate. The average LHaC of the adult group (Figure 3c) within the alpha band peaked at around 12 Hz and had a longer decay rate compared with the two infant groups, indicating an increase in both alpha peak frequency and rhythmicity between infancy and adulthood.

To determine if there were any differences in spectral rhythmicity between the observation and execution conditions, and between the baseline and the task-related epochs, a mass-univariate two-way repeated measures ANOVA was applied to LHaC for each group with condition, epoch, and their interaction as factors (see Methods). The 9-month infant group (Figure 3d) exhibited only one small, significant LHaC cluster for the condition by epoch interaction in the alpha band at 5 Hz and from 1.1 to 1.2 cycles, whereas this effect was observed in the 12-month infants (Figure 3e) at around 8 Hz and from 0.2 to 2.0 cycles, and in adults (Figure 3f) at around 10Hz and from 0.2 to 2.5 cycles. The 12-month group also exhibited significant LHaC clusters for the condition by epoch interaction in the beta band around 10 Hz and from 0.05 to 0.25 cycles, and the gamma band (18-50 Hz) from 0.05 to 0.5 cycles. In the adult group, the condition by epoch LHaC interaction effect was apparent in the theta band (5-8 Hz) from 0.05 to 1 cycle, beta band from 15 to 18 Hz and from 0.1 to 0.25 cycles, and the gamma band (28-50 Hz) from 0.05 to 0.9 cycles. The range of frequency bands and lag cycles in which LHaC was differentially modulated by task conditions and epochs therefore expanded from between infancy and adulthood.

We then followed up these significant interaction effects with pairwise comparisons between conditions within each epoch. This revealed significant between-condition differences in LHaC within the 12-month group in the epochs aligned to the start of the grasp, grasp completion, and the end of the movement (Figure 3g). In each of these epochs, alpha LHaC at around 8 Hz was lower in the execution compared to the observation condition (go-cue execution: M = 0.21; go-

cue observation: *M* = 0.33; cluster size = 83, *p* = 0.029; grasp-complete execution: *M* = 0.27; grasp-complete observation: *M* = 0.41; cluster size = 81, *p* = 0.032; movement-end execution: *M* = 0.19; task-end observation: *M* = 0.30; cluster size = 176, *p* = 0.043), and across increasingly longer lags over epochs. Small clusters of greater beta LHaC at very short lags for execution compared to observation were detected in the go-cue epoch (10-13 Hz; 0.05 - 0.5 cycles; execution: *M* = 0.43; observation: *M* = 0.33; cluster size = 72, *p* = 0.035), and the grasp-complete epoch (execution: *M* = 0.33; observation: *M* = 0.24; cluster size = 112, *p* = 0.017). In the gamma band (18-47 Hz), LHaC was higher during execution from 0.05 to 1 cycle in the grasp-complete (execution: *M* = 0.25; observation: *M* = 0.16; cluster size = 709, *p* = 0.001) and movement-end (execution: *M* = 0.25; observation: *M* = 0.17; cluster size = 662, *p* = 0.035) epochs. In contrast, LHaC in the adult group only differed between conditions in the theta and alpha bands during these epochs. Similar to the 12-month group, adult LHaC in the alpha band (~10 Hz) was lower in the execution compared to the observation condition during the grasp-complete and the movement-end epochs (Figure 3h; go-cue execution: *M* = 0.10; go-cue observation: *M* = 0.23; cluster size = 190, *p* = 0.037; grasp-complete execution: *M* = 0.09; grasp-complete observation: *M* = 0.21; cluster size = 210, *p* = 0.038; movement-end execution: *M* = 0.11; movement-end observation: *M* = 0.27; cluster size = 245, *p* = 0.022). Additionally, adult LHaC in the theta band was higher during execution compared to observation condition in the movement-end epoch (movement-end execution: *M* = 0.28; movement-end observation: *M* = 0.20; cluster size = 150, *p* = 0.043). In summary, whereas alpha was less rhythmic during execution than observation in both 12-month-olds and adults, beta and gamma were more rhythmic during execution in 12-month-olds, and theta was more rhythmic after movement performance in adults.

We also performed follow-up pairwise comparisons between epochs within each condition. Notably, between-epoch differences were only found in the execution condition and for the adult group, with lower alpha LHaC (~10 Hz) in task-related epochs compared to the baseline epoch across the entire range of lags tested (Figure 3i; 0.1 - 4.2 cycles; go-cue epoch: *M* = 0.11; baseline: *M* = 0.23; cluster size = 300, *p* = 0.017; grasp-complete epoch: *M* = 0.10; baseline: *M* = 0.23; cluster size = 327, *p* = 0.015; movement-end epoch: *M* = 0.11; baseline: *M* = 0.24; cluster size = 358, *p* = 0.011). Increases in LHaC were found in the grasp-complete and movement-end epochs compared with baseline in the gamma band (grasp-complete epoch: *M* = 0.53; baseline: *M* = 0.40; cluster size = 188, *p* = 0.038; movement-end epoch: *M* = 0.49; baseline: *M* = 0.37; cluster size = 252, *p* = 0.017). In adults, alpha therefore became less rhythmic during action execution, whereas gamma became more rhythmic during and after movement.

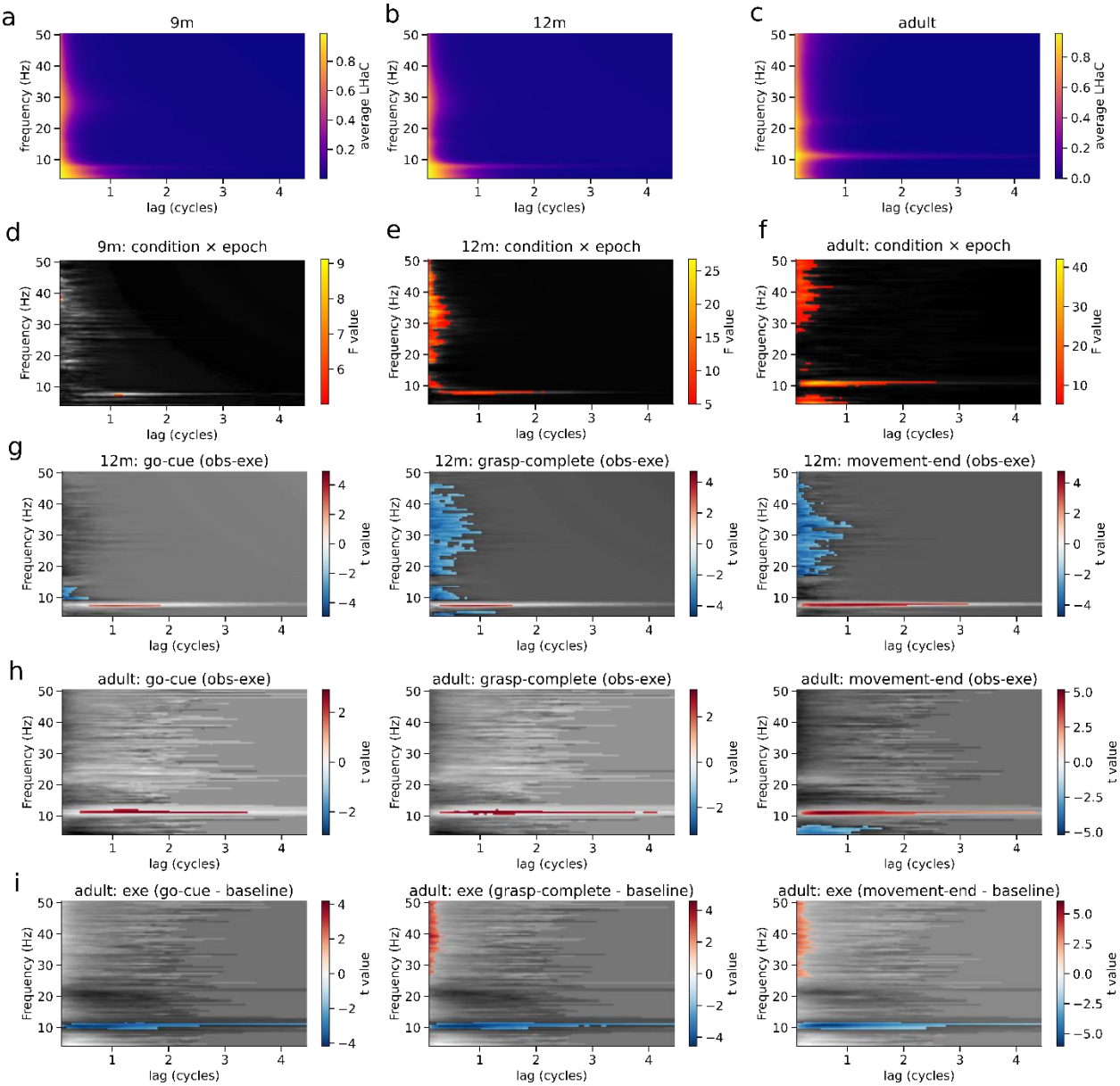

Figure 3. Sensorimotor rhythmicity differs between action execution and observation. a-c) Group-averaged lagged Hilbert autocoherence (LHaC) computed within EEG electrode clusters over sensorimotor cortex from 9-month, 12-month infants and adults. Alpha peak frequency and rhythmicity increases with age. d-f) LHaC F statistics for the condition by epoch interaction for each group. Statistically significant clusters, corrected using cluster-based permutation tests, are shown in color. g) LHaC T-statistics for epochs (aligned to the go-cue, grasp completion, and end of the movement) with between-condition differences for the 12-month infants. h) and i) LHaC T-statistics for epochs with between-condition and between-epoch differences, respectively, for the adult group.

3.3 Alpha and beta rhythmicity index implicit sensorimotor adaptation over blocks of trials

Having demonstrated the utility of lagged Hilbert autocoherence for evaluating condition and epoch differences in sensorimotor rhythmicity averaged over trials, we then applied it to investigate dynamic shifts rhythmicity over blocks of trials. Specifically, we examined changes in alpha and beta rhythmicity in the context of sensorimotor learning. We computed LHaC from MEG

data acquired during a visuomotor adaptation task (Szul et al., 2023), focusing on a cluster of sensors centered over the left sensorimotor cortex. Two groups of subjects performed joystick-based reaches with their right hand to visually presented targets after observing a random dot kinematogram with varying levels of coherent rotational motion in either the clockwise or counter-clockwise direction. In some trials, the position of the cursor controlled by the joystick was rotated 30 degrees relative to the actual movement of the joystick. For the implicit group, the rotation was always 30 degrees counter-clockwise and was unrelated to the direction of coherent motion in the RDK. These subjects could therefore compensate for the rotation using implicit sensorimotor adaptation (Taylor et al., 2014). For the explicit group, the direction of the rotation was entirely predicted by the direction of RDK coherent motion, and when there was no coherent motion there was no rotation. The optimal strategy for this group was therefore to use an explicit re-aiming strategy to compensate for the predicted perturbation (Taylor et al., 2014). After an initial training, each group completed one baseline block of trials, six blocks with visuomotor rotation, and one wash-out block.

Averaged across rotation blocks, the implicit and explicit groups had comparable patterns of lagged autocoherence across frequencies and lags in both the visual (Figure 4a,b) and motor (Figure 4g,h) epochs. We examined block-by-block differences (relative to the baseline block) between groups in the alpha and beta frequency bands, specifically at 3 cycles for alpha and 1 cycle for beta, as well as total lagged autocoherence within each band across all cycles. During the visual epochs, there were no significant intergroup differences in alpha LHaC in any block (Figure 4c, d), but beta LHaC at 1 cycle and total beta LHaC both had a contrasting trajectory between the groups, resulting in intergroup differences in most of the rotation blocks (Figure 4e, f; beta LHaC at 1 cycle: block 2, $p = 0.031$, block 3, $p = 0.005$; total beta LHaC: block 3, $p = 0.012$, block 5, $p = 0.032$). In contrast to the visual epochs, there were pronounced group differences in alpha and beta LHaC in the motor epochs. Alpha LHaC at 3 cycles was higher in the implicit group during most of the rotation blocks (Figure 4i; block 3, $p = 0.003$; block 4, $p = 0.001$; block 5, $p = 0.004$; block 7, $p = 0.009$), whereas total alpha LHaC increased in both groups during the rotation blocks, albeit more quickly in the implicit group, resulting in higher total alpha LHaC in the implicit group for the first three rotation blocks (Figure 4j; block 2, $p = 0.002$; block 3, $p = 0.007$; block 4, $p = 0.001$). Beta LHaC, both at 1 cycle and total over all cycles, increased in the implicit group during the rotation blocks, subsequently reverting to baseline during the wash-out block, but remained relatively static over the course of the experiment in the explicit group (Figure 4k, l; beta LHaC at 1 cycle: block 2, $p = 0.037$, block 3, $p = 0.003$, block 4, $p = 0.017$, block 5, $p = 0.043$, block 7, $p = 0.031$; total beta LHaC: block 3, $p = 0.007$, block 4, $p = 0.007$, block 5, $p = 0.046$). In summary, there were no significant intergroup differences during the visual epoch in sensorimotor alpha rhythmicity. However, during the motor epoch, alpha rhythmicity increased in both groups over the course of the experiment, with a marked accentuation beginning with the first rotation block in the implicit group. Beta rhythmicity, in contrast, differed between groups in that it sharply increased only in the implicit group during the rotation blocks and returned to baseline in the wash-out block.

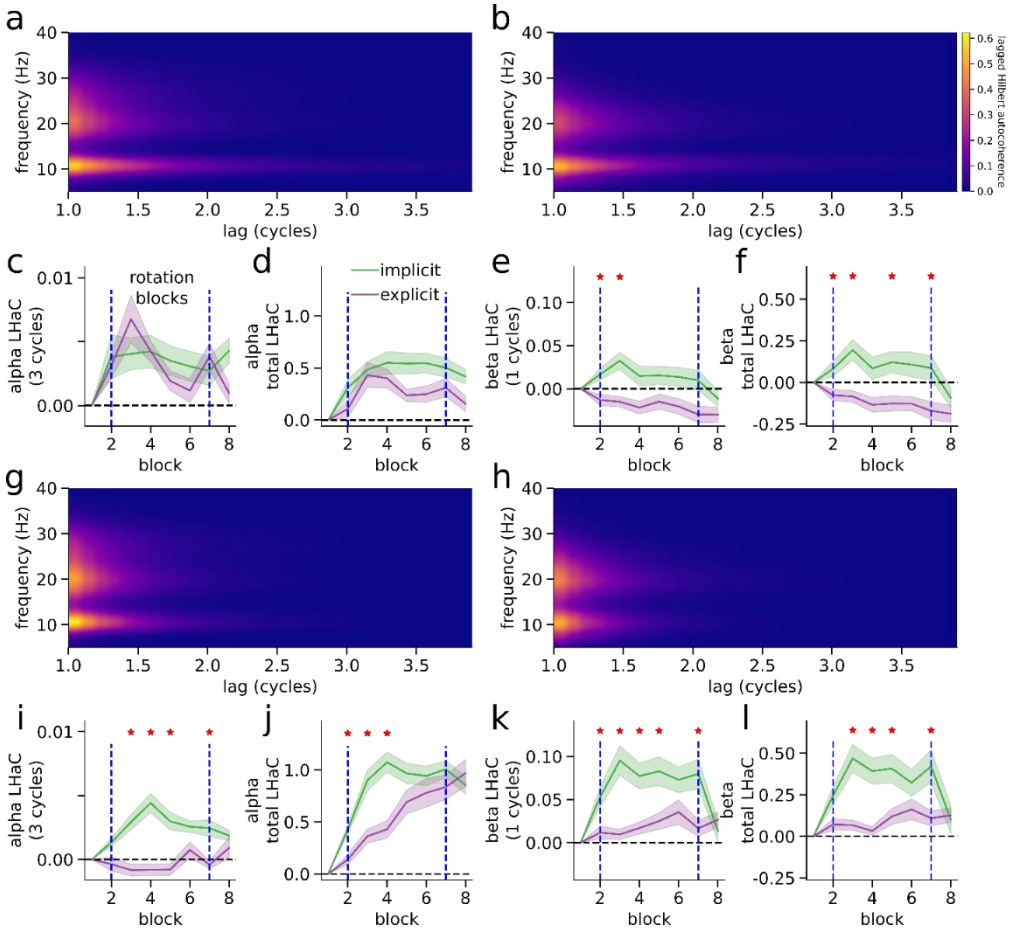

Figure 4. Alpha and beta rhythmicity during sensorimotor learning. a) Lagged Hilbert autocoherence in left central sensors for the visual epoch in the implicit group, averaged over visuomotor rotation blocks. b) As in (a), for the explicit group. c) Alpha LHaC at a lag of 3 cycles, for the visual epoch in each block. The solid lines indicate the mean value over subjects for the implicit (green) and explicit (purple) groups and the shaded areas represent the standard error. The vertical dashed lines indicate the beginning and end of the rotation blocks. d) As in (c), for the total alpha LHaC. e) As in (c), for beta LHaC at a lag of 1 cycle. Red stars indicate blocks in which LHaC was significantly different between the two groups. f) As in (c), for the total beta LHaC. g) Lagged Hilbert autocoherence in left central sensors for the motor epoch in the implicit group, averaged over visuomotor rotation blocks. h) As in (g), for the explicit group. i) As in (c), for alpha LHaC at a lag of 3 cycles in the motor epoch. j) As in (i), for the total alpha LHaC. k) As in (i), for beta LHaC at a lag of 1 cycle, l) As in (i), for the total beta LHaC.

3.4 Beta rhythmicity in primary motor cortex predicts trial-by-trial response time

We then narrowed our focus from blocks of trials to using rhythmicity, specifically in the beta band, to predict trial-by-trial behavior. Lagged Hilbert autocoherence was calculated in each trial from bi-hemispheric LFP recordings made in the primary motor cortex of two macaque monkeys (Dixon et al., 2021). The trial-averaged lagged Hilbert autocoherence of one example session from one monkey is shown in Figure 5a. In all sessions from both monkeys, the only prominent peak in LHaC was in the beta frequency range (20-28 Hz), and beta LHaC decayed with increasing lag cycles, reaching half its maximum value at around 0.5 - 1.5 lag cycles.

We then tested the ability to predict response time (RT) from total beta LHaC (summed over all evaluated lags) in each hemisphere in 1s epochs defined relative to the go cue (Figure 5b, inset).

There was no significant main effect of hemisphere (contralateral versus ipsilateral) or an interaction between hemisphere and total LHaC in any tested epoch. However, the main effect of total beta LHaC on RT increased with the epoch start time, with a significant main effect found at epochs starting at -1s (β_{LHaC} = 0.0015, p = 0.024), -0.75s (β_{LHaC} = 0.0028, p < 0.0001), -0.5s (β_{LHaC} = 0.0038, p < 0.0001), -0.25 s (β_{LHaC} = 0.0064, p < 0.0001), and 0 s (β_{LHaC} = 0.0114, p < 0.0001) relative to the go cue (Figure 5b). We further examined correlations between total beta LHaC in each hemisphere and RT within each session of both monkeys, focusing on the final 1s epoch aligned to the go cue (Figure 5b, red circle). Total beta LHaC was significantly correlated with RT in most sessions contralaterally (monkey 1: 8/13, see example session in Figure 5c: r = 0.118, p=0.001; monkey 2: 4/7; r = 0.074 - 0.242, all p < 0.05), and in approximately half of the sessions ipsilaterally (monkey 1: 6/13, see example session in Figure 5d: r = 0.131, p < 0.001; monkey 2: 3/7; r = 0.072 - 0.131, all p < 0.05). All significant total beta LHaC coefficients were greater than zero, indicating that increased beta rhythmicity in contralateral, and to a lesser extent ipsilateral, primary motor cortex predicted slower RTs. Moreover, this effect increased in the time preceding the go cue.

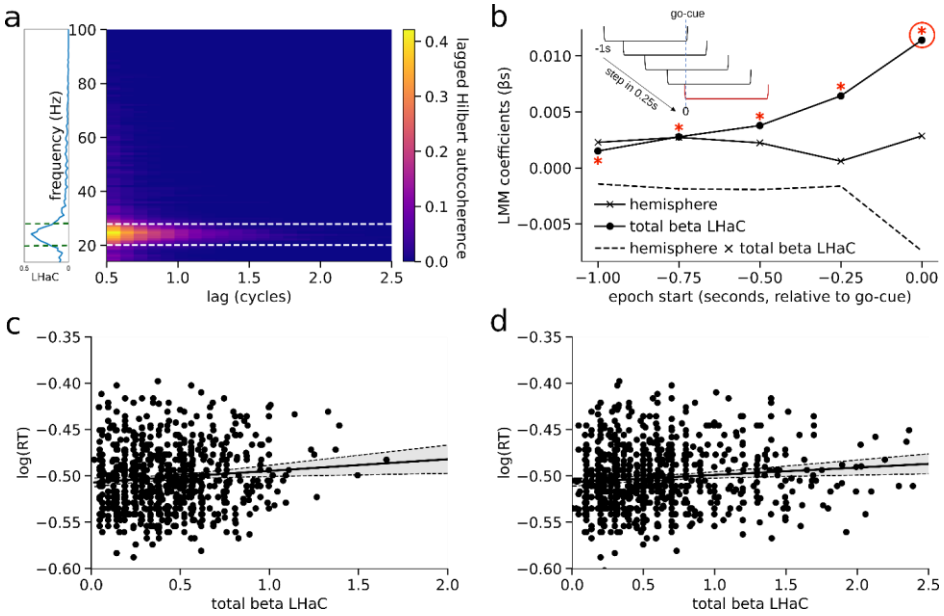

Figure 5. Beta lagged Hilbert autocoherence predicts response time. a) The trial-averaged lagged Hilbert autocoherence (LHaC) in one example session from the LFP data of one monkey. The vertical plot on the left how the beta frequency range is determined by the full width at half maximum (FWHM) of lagged autocoherence at 0.5 cycles. The frequency range between the two dashed lines corresponds to the beta band range used in our analyses. b) The estimated coefficients (βs) of linear mixed models fit to total beta LHaC computed in 1s epochs aligned from 1s, 0.75s, 0.5s, 0.25s, and 0s prior to the go cue (inset). The significant effects are indicated with red stars, and the epoch selected for examining correlations between total beta LHaC and RT is indicated with a red circle. d) and e) Example sessions in which total beta LHaC is correlated with RT in the contralateral (d) or ipsilateral (e) hemisphere.

4. Discussion

In this paper we introduced a novel algorithm, lagged Hilbert autocoherence (LHaC), to characterize the rhythmicity of neuronal oscillations. We have shown how LHaC, a refinement of lagged Fourier autocoherence (LFaC; Fransen et al., 2016, 2015), can provide the sensitivity and

accuracy required to probe differences in neural rhythmicity between conditions, between subject groups over blocks of trials, and single trial relationships between rhythmicity and behavior. LFaC has been used to demonstrate differences in rhythmicity between frequency bands (Fransen et al., 2016; Little et al., 2019; Szul et al., 2023), and between experimental conditions or subject groups within a frequency band (Rayson et al., 2023, 2022). However, it suffers from poor spectral accuracy and resolution, aliasing effects at higher frequencies, and conflation with amplitude covariations. In contrast, the precise bandpass filtering used by LHaC yields lagged autospectra with peaks that closely match the periodic frequency peaks in PSDs. We validated these improvements in simulation, and have shown how these properties can be leveraged to show that sensorimotor rhythmicity, in the alpha and beta frequency bands, differs between conditions and epochs during action observation and execution, changes in distinct ways during implicit and explicit sensorimotor learning, and predicts response times in a reaching task.

Using EEG data, we found an increase in both alpha peak frequency and rhythmicity between infancy and adulthood, corresponding to what has been found previously using LFaC (Rayson et al., 2023, 2022). In line with task-related changes that have previously been described for alpha power (Aleksandrov and Tugin, 2012; Debnath et al., 2019), alpha was less rhythmic during action execution than observation in all age groups. Our simulation results suggest that, in addition to reduced alpha oscillation amplitude, this reflects shorter bouts of alpha oscillations during action execution (Schaworonkow and Voytek, 2021). In contrast to alpha, beta and gamma rhythmicity were only modulated in 12-month-olds and adults, with the greatest increases occurring toward the end of the movement. These increases may correspond to the post-movement beta rebound (Cassim et al., 2000; Cheyne, 2013; Jurkiewicz et al., 2006) and movement-related gamma synchrony (Cheyne et al., 2008; Muthukumaraswamy, 2010), which are increases in beta and gamma power, but both have only been observed in older children and adults (Gaetz et al., 2020, 2010; Hao et al., 2019). Nevertheless, signal rhythmicity and power can vary independently (van Ede et al., 2018), and therefore LHaC may be a more sensitive measure of age-related changes in frequency-specific neural activity compared to power. We also ran the same analysis using LFaC (Figure S2), and whilst the overall averaged lagged autocoherence maps were broadly similar, the clusters of significant condition by epoch differences were very coarse, and shifted in frequency with increasing lags.

In the sensorimotor adaptation task with adults, alpha rhythmicity increased in both groups during the motor epoch over the course of the experiment, but with a more abrupt increase for the implicit group during the first rotation block. This could be related to more general error processing mechanisms (Driel et al., 2012; Navarro-Cebrian et al., 2013). However, beta rhythmicity sharply increased only in the implicit group during the rotation blocks and returned to baseline in the wash-out block, whereas it remained relatively static in the explicit group. Beta rhythmicity therefore may be a marker of implicit sensorimotor adaptation (Jahani et al., 2020), possibly driven by bursts with distinct waveform shapes in the beta rebound period (Szul et al., 2023). In order to determine if these differences in rhythmic neural activity associated with implicit and explicit learning mechanisms could be observed with LFaC, we computed this from the same dataset, using the same range of frequencies and lags. LFaC revealed similar patterns of changes in alpha and beta rhythmicity over the course of the experiment, but was much less sensitive to group differences, especially in the beta range (Figure S3).

In the monkey LFP data, relative beta power was strongest in the deepest layers, and the spectrolaminar motif observed closely resembled that described in visual and prefrontal regions (Figure S1; Mendoza-Halliday et al., 2024). We therefore focused on the relationship between beta LHaC in these layers and behavior, but in the future LHaC could be used to further characterize spectrolaminar motifs in terms of relative rhythmicity rather than power. We found that increased beta rhythmicity in contralateral, and to a lesser extent ipsilateral, primary motor cortex predicted slower response times (RTs), and this effect increased in the time preceding the go cue. This is likely driven, at least in part, by the previously shown relationships between burst timing and RT (Little et al., 2019), but may also suggest a relationship with burst duration and waveform and RT. We also tested the ability to predict RT from LFaC and found main effects of hemisphere and LFaC in each epoch, but with lower coefficient values than for LHaC that did not monotonically increase over time (Figure S4).

Whilst this approach discards the assumption of phase consistency over time, it still assumes stationarity in peak frequency. LHaC and related methods, therefore, cannot detect rhythmic signals that change in peak frequency. However, we know that there are changes in instantaneous frequency in some signals (Benwell et al., 2019; Nelli et al., 2017) which are difficult to track using methods based on bandpass filtering. Variants of empirical mode decomposition have been proposed to separate neural signals into modes which may vary in instantaneous frequency (Fabus et al., 2021; Huang et al., 1998; Quinn et al., 2021b, 2021a), thereby isolating signal sources that are mixed together in sensor signals. An interesting future direction would therefore be to adapt LHaC to apply to each mode derived from EMD in order to examine changes in rhythmicity of frequency-varying neural activity.

One of the strengths of our approach is spectral precision, which results from narrow bandpass filtering. However, this also reflects a potential weakness: in frequency ranges with low power, narrow bandpass filtering introduces amplitude correlations which result in spuriously high lagged autocoherence. Another approach could be to focus exclusively on the phase, using lagged phase-locking value (Bruña et al., 2018; Lachaux et al., 2000). This approach was used in a recent study (Myrov et al., 2024), whereby ‘rhythmicity’ was quantified using a phase-autocorrelation function (pACF) derived from the phase-locking value. However, this necessitated a correction of the signal lag using the mean instantaneous frequency of the narrow-band signal to avoid a bias towards higher frequencies. In contrast, we used a threshold computed from surrogate data generated from an autoregressive model, which has the advantage that the metric is thus adapted to the SNR of the dataset (Brookshire, 2022).

The recent surge in sophisticated techniques for analyzing frequency-specific neural activity has been largely fueled by a growing appreciation of the potential for activity in some frequency ranges, most notably beta and gamma, to manifest not as continuous oscillations, but as discrete, transient bursts (Feingold et al., 2015; Lundqvist et al., 2016; Sherman et al., 2016). The validity of this notion could radically reshape theories anchored in the concept of phase precession of oscillatory activity being perpetuated over extended time intervals. Conversely, the appearance of burst-like activity could be an artifact of our recording methods, only made visible when the amplitude crosses a certain detectability threshold, with the actual activity being driven by an underlying rhythmic process (van Ede et al., 2018). Lagged coherence has previously been used

to discern whether activity within a specific frequency band is "bursty" or oscillatory (Fransen et al., 2016; Little et al., 2019; Rayson et al., 2023, 2022; Szul et al., 2023), but detection of bursts has predominantly relied on power measurements (Brady and Bardouille, 2022; Rayson et al., 2022; Shin et al., 2017; Szul et al., 2023; though see Cole and Voytek, 2019). A temporally-resolved version of lagged Hilbert autocoherence could be used to detect frequency-specific, oscillatory bursts by running the algorithm time-point by time-point, and calculating LHaC between each time point and the point 0.5 cycles into the future. This approach could enable a more precise characterization of each burst's onset and offset and the detection of purely oscillatory bursts.

Algorithms that effectively parameterize the periodic and aperiodic components of power spectral densities (Barry and Blasio, 2021; Donoghue et al., 2020; Gerster et al., 2022; Wen and Liu, 2016) have sparked significant advances in systems and cognitive neuroscience, transitioning the field away from the conventional tendency to conflate these two distinct signal sources. Benefiting from these algorithms, numerous studies have found that task-specific modulation of aperiodic activity can provide crucial insight into cognitive processing (Waschke et al., 2021), shifts in the slope of aperiodic activity can index excitation/inhibition balance (Gao et al., 2017), and abnormal periodic and aperiodic activity can serve as early indicators of neurodegenerative diseases (Karalunas et al., 2022; Ostlund et al., 2021). Despite their evident value, these methodologies rely on the presumption that neural signals can be cleanly partitioned into rhythmic (periodic) and arhythmic (aperiodic) components based solely on the shape of the power spectral density (PSD). They thus operate under the assumption that a 1/f model of aperiodic activity can be robustly fit to the power spectral density (PSD), and then periodic activity can be parameterized from the residuals of this fit. Two key advantages of LHaC could be leveraged in order to simultaneously fit both the aperiodic and periodic components of the PSDs. The first advantage is the method's high spectral accuracy and resolution, which can match that of the PSD. The second advantage is that, at short lags, lagged Hilbert autocoherence is, by definition, proportional to the periodic component of the PSD. Fits generated using this approach could significantly reduce the number of "missed" periodic peaks and spurious high frequency peaks, leading to a more accurate and robust analysis of neural power spectra.

5. Conclusion

In conclusion, the present study introduces lagged Hilbert autocoherence (LHaC) as a refined approach for measuring neural rhythmicity, addressing key limitations of Fourier-based autocoherence (LFaC). Via simulations and application across EEG, MEG, and LFP data, we demonstrate the versatility and sensitivity of LHaC in capturing condition-specific and age-related rhythmic changes, learning-related adaptations, and trial-specific behavioral associations. By enhancing spectral precision and accommodating the minimization of spurious coherence, LHaC provides a valuable tool for advancing the study of neural oscillatory dynamics.

Acknowledgements

This research was supported by grants from the European Research Council (ERC) under the European Union’s Horizon 2020 research and innovation programme (ERC consolidator grant 864550), and the French National Research Agency (ANR) project HiFi (2020–2024, ANR-20-CE17-0023). The funders had no role in the preparation of the manuscript.

References

Akaike, H., 1974. A new look at the statistical model identification. IEEE Trans. Automat. Control AC-19, 716–723.

Akaike, H., 1973. Information theory and an extension of the maximum likelihood principle, in: Petrov, B.N., Csaki, F. (Eds.), 2nd Internat. Symp. on Information Theory. Akademia Kiado, Budapest, pp. 267–281.

Aleksandrov, A.A., Tugin, S.M., 2012. Changes in the Mu Rhythm in Different Types of Motor Activity and on Observation of Movements. Neurosci Behav Physi 42, 302–307. https://doi.org/10.1007/s11055-012-9566-2

Barry, R.J., Blasio, F.M.D., 2021. Characterizing pink and white noise in the human electroencephalogram. J. Neural Eng. 18, 034001. https://doi.org/10.1088/1741-2552/abe399

Benwell, C.S.Y., London, R.E., Tagliabue, C.F., Veniero, D., Gross, J., Keitel, C., Thut, G., 2019. Frequency and power of human alpha oscillations drift systematically with time-on-task. NeuroImage 192, 101–114. https://doi.org/10.1016/j.neuroimage.2019.02.067

Bonnefond, M., Kastner, S., Jensen, O., 2017. Communication between Brain Areas Based on Nested Oscillations. eNeuro 4.

Brady, B., Bardouille, T., 2022. Periodic/Aperiodic parameterization of transient oscillations (PAPTO)–Implications for healthy ageing. NeuroImage 251, 118974. https://doi.org/10.1016/j.neuroimage.2022.118974

Brookshire, G., 2022. Putative rhythms in attentional switching can be explained by aperiodic temporal structure. Nat Hum Behav 6, 1280–1291. https://doi.org/10.1038/s41562-022-01364-0

Bruña, R., Maestú, F., Pereda, E., 2018. Phase locking value revisited: teaching new tricks to an old dog. J. Neural Eng. 15, 056011. https://doi.org/10.1088/1741-2552/aacfe4

Buzsáki, G., Freeman, W., 2015. Brain rhythms and dynamic coordination. Current Opinion in Neurobiology 31, 5–9. https://doi.org/10.1016/j.conb.2015.01.016

Cannon, E.N., Yoo, K.H., Vanderwert, R.E., Ferrari, P.F., Woodward, A.L., Fox, N.A., 2014. Action Experience, More than Observation, Influences Mu Rhythm Desynchronization. PLOS ONE 9, e92002. https://doi.org/10.1371/journal.pone.0092002

Carter, G., 1977. Receiver operating characteristics for a linearly thresholded coherence estimation detector. IEEE Transactions on Acoustics, Speech, and Signal Processing 25, 90–92.

Cassim, F., Szurhaj, W., Sediri, H., Devos, D., Bourriez, J.L., Poirot, I., Derambure, P., Defebvre, L., Guieu, J.D., 2000. Brief and sustained movements: Differences in event-related (de)synchronization (ERD/ERS) patterns. Clinical Neurophysiology 111, 2032–2039. https://doi.org/10.1016/S1388-2457(00)00455-7

Cheyne, D., Bells, S., Ferrari, P., Gaetz, W., Bostan, A.C., 2008. Self-paced movements induce high-frequency gamma oscillations in primary motor cortex. NeuroImage 42, 332–342.

Cheyne, D.O., 2013. MEG studies of sensorimotor rhythms: A review. Experimental Neurology 245, 27–39. https://doi.org/10.1016/J.EXPNEUROL.2012.08.030

Cohen, D., Tsuchiya, N., 2018. The Effect of Common Signals on Power, Coherence and Granger Causality: Theoretical Review, Simulations, and Empirical Analysis of Fruit Fly LFPs Data. Front Syst Neurosci 12, 30. https://doi.org/10.3389/fnsys.2018.00030

Cole, S., Voytek, B., 2019. Cycle-by-cycle analysis of neural oscillations. Journal of neurophysiology 122, 849–861. https://doi.org/10.1152/jn.00273.2019

de Cheveigné, A., 2020. ZapLine: A simple and effective method to remove power line artifacts. NeuroImage 207, 116356. https://doi.org/10.1016/j.neuroimage.2019.116356

Debnath, R., Buzzell, G.A., Morales, S., Bowers, M.E., Leach, S.C., Fox, N.A., 2020. The Maryland analysis of developmental EEG (MADE) pipeline. Psychophysiology 57, e13580. https://doi.org/10.1111/psyp.13580

Debnath, R., Salo, V.C., Buzzell, G.A., Yoo, K.H., Fox, N.A., 2019. Mu rhythm desynchronization is specific to action execution and observation: Evidence from time-frequency and connectivity analysis. NeuroImage 184, 496–507. https://doi.org/10.1016/j.neuroimage.2018.09.053

Dixon, T.C., Merrick, C.M., Wallis, J.D., Ivry, R.B., Carmena, J.M., 2021. Hybrid dedicated and distributed coding in PMd/M1 provides separation and interaction of bilateral arm signals. PLOS Computational Biology 17, e1009615. https://doi.org/10.1371/journal.pcbi.1009615

Donoghue, T., Haller, M., Peterson, E.J., Varma, P., Sebastian, P., Gao, R., Noto, T., Lara, A.H., Wallis, J.D., Knight, R.T., Shestyuk, A., Voytek, B., 2020. Parameterizing neural power spectra into periodic and aperiodic components. Nat Neurosci 23, 1655–1665. https://doi.org/10.1038/s41593-020-00744-x

Donoghue, T., Schaworonkow, N., Voytek, B., 2022. Methodological considerations for studying neural oscillations. European Journal of Neuroscience 55, 3502–3527. https://doi.org/10.1111/ejn.15361

Driel, J. van, Ridderinkhof, K.R., Cohen, M.X., 2012. Not All Errors Are Alike: Theta and Alpha EEG Dynamics Relate to Differences in Error-Processing Dynamics. J. Neurosci. 32, 16795–16806. https://doi.org/10.1523/JNEUROSCI.0802-12.2012

Fabus, M.S., Quinn, A.J., Warnaby, C.E., Woolrich, M.W., 2021. Automatic decomposition of electrophysiological data into distinct non-sinusoidal oscillatory modes. bioRxiv 2021.07.06.451245. https://doi.org/10.1101/2021.07.06.451245

Feingold, J., Gibson, D.J., DePasquale, B., Graybiel, A.M., 2015. Bursts of beta oscillation differentiate postperformance activity in the striatum and motor cortex of monkeys performing movement tasks. Proceedings of the National Academy of Sciences of the United States of America 112, 13687–92. https://doi.org/10.1073/pnas.1517629112

Fox, J., Weisberg, S., Price, B., Adler, D., Bates, D., Baud-Bovy, G., Bolker, B., 2019. car: Companion to Applied Regression. R package version 3.0-2. Website https://CRAN. R-project. org/package= car [accessed 17 March 2020].

Fransen, A.M.M., Dimitriadis, G., van Ede, F., Maris, E., 2016. Distinct α- and β-band rhythms over rat somatosensory cortex with similar properties as in humans. Journal of Neurophysiology 115, 3030–3044. https://doi.org/10.1152/jn.00507.2015

Fransen, A.M.M., van Ede, F., Maris, E., 2015. Identifying neuronal oscillations using rhythmicity. NeuroImage 118, 256–267. https://doi.org/10.1016/j.neuroimage.2015.06.003

Fries, P., 2015. Rhythms for Cognition: Communication through Coherence. Neuron 88, 220–235. https://doi.org/10.1016/j.neuron.2015.09.034

Gaetz, W., MacDonald, M., Cheyne, D., Snead, O.C., 2010. Neuromagnetic imaging of movement-related cortical oscillations in children and adults: Age predicts post-movement beta rebound. NeuroImage 51, 792–807. https://doi.org/10.1016/j.neuroimage.2010.01.077

Gaetz, W., Rhodes, E., Bloy, L., Blaskey, L., Jackel, C.R., Brodkin, E.S., Waldman, A., Embick, D., Hall, S., Roberts, T.P.L., 2020. Evaluating motor cortical oscillations and age-related change in autism spectrum disorder. NeuroImage 207, 116349. https://doi.org/10.1016/J.NEUROIMAGE.2019.116349

Gallet, C., Julien, C., 2011. The significance threshold for coherence when using the Welch's periodogram method: effect of overlapping segments. Biomedical Signal Processing and Control 6, 405–409.

Gao, R., Peterson, E.J., Voytek, B., 2017. Inferring synaptic excitation/inhibition balance from field potentials. NeuroImage 158, 70–78. https://doi.org/10.1016/j.neuroimage.2017.06.078

Gerster, M., Waterstraat, G., Litvak, V., Lehnertz, K., Schnitzler, A., Florin, E., Curio, G., Nikulin, V., 2022. Separating Neural Oscillations from Aperiodic 1/f Activity: Challenges and Recommendations. Neuroinform 20, 991–1012. https://doi.org/10.1007/s12021-022-09581-8

Gramfort, A., Luessi, M., Larson, E., Engemann, D.A., Strohmeier, D., Brodbeck, C., Parkkonen, L., Hämäläinen, M.S., 2014. MNE software for processing MEG and EEG data. NeuroImage 86, 446–460. https://doi.org/10.1016/j.neuroimage.2013.10.027

Hao, J., Feng, W., Zhang, L., Liao, Y., 2019. The Post-Movement Beta Rebound and Motor-Related Mu Suppression in Children. https://doi.org/10.1080/00222895.2019.166276252, 590–600. https://doi.org/10.1080/00222895.2019.1662762

Hu, M., Liang, H., 2012. Noise-Assisted Instantaneous Coherence Analysis of Brain Connectivity. Computational Intelligence and Neuroscience 2012, e275073. https://doi.org/10.1155/2012/275073

Huang, N.E., Shen, Z., Long, S.R., Wu, M.C., Shih, H.H., Zheng, Q., Yen, N.-C., Tung, C.C., Liu, H.H., 1998. The empirical mode decomposition and the Hilbert spectrum for nonlinear and non-stationary time series analysis. Proceedings of the Royal Society of London. Series A: Mathematical, Physical and Engineering Sciences 454, 903–995. https://doi.org/10.1098/RSPA.1998.0193

Jahani, A., Schwey, A., Bernier, P.-M., Malfait, N., 2020. Spatially Distinct Beta-Band Activities Reflect Implicit Sensorimotor Adaptation and Explicit Re-aiming Strategy. J. Neurosci. 40, 2498–2509. https://doi.org/10.1523/JNEUROSCI.1862-19.2020

Jensen, O., Bonnefond, M., Marshall, T.R., Tiesinga, P., 2015. Oscillatory mechanisms of feedforward and feedback visual processing. Trends in Neurosciences 38, 192–194. https://doi.org/10.1016/j.tins.2015.02.006

Jurkiewicz, M.T., Gaetz, W.C., Bostan, A.C., Cheyne, D., 2006. Post-movement beta rebound is generated in motor cortex: Evidence from neuromagnetic recordings. NeuroImage 32, 1281–1289.

Karalunas, S.L., Ostlund, B.D., Alperin, B.R., Figuracion, M., Gustafsson, H.C., Deming, E.M., Foti, D., Antovich, D., Dude, J., Nigg, J., Sullivan, E., 2022. Electroencephalogram aperiodic power spectral slope can be reliably measured and predicts ADHD risk in early development. Developmental Psychobiology 64, e22228. https://doi.org/10.1002/dev.22228

Kumaravel, V.P., Farella, E., Parise, E., Buiatti, M., 2022. NEAR: An artifact removal pipeline for human newborn EEG data. Developmental Cognitive Neuroscience 54, 101068. https://doi.org/10.1016/j.dcn.2022.101068

Lachaux, J.-P., Rodriguez, E., Le Van Quyen, M., Lutz, A., Martinerie, J., Varela, F.J., 2000. Studying single-trials of phase synchronous activity in the brain. International Journal of Bifurcation and Chaos 10, 2429–2439.

Le Van Quyen, M., Foucher, J., Lachaux, J.-P., Rodriguez, E., Lutz, A., Martinerie, J., Varela, F.J., 2001. Comparison of Hilbert transform and wavelet methods for the analysis of neuronal synchrony. Journal of Neuroscience Methods 111, 83–98. https://doi.org/10.1016/S0165-0270(01)00372-7

Leach, S.C., Morales, S., Bowers, M.E., Buzzell, G.A., Debnath, R., Beall, D., Fox, N.A., 2020. Adjusting ADJUST: Optimizing the ADJUST algorithm for pediatric data using geodesic nets. Psychophysiology 57, e13566. https://doi.org/10.1111/psyp.13566

Little, S., Bonaiuto, J., Barnes, G., Bestmann, S., 2019. Human motor cortical beta bursts relate to movement planning and response errors. PLOS Biology 17, e3000479. https://doi.org/10.1371/journal.pbio.3000479

Lundqvist, M., Rose, J., Herman, P., Brincat, S.L., Buschman, T.J., Miller, E.K., 2016. Gamma and Beta Bursts Underlie Working Memory. Neuron 90, 152–164. https://doi.org/10.1016/J.NEURON.2016.02.028

Mann, M.E., Lees, J.M., 1996. Robust estimation of background noise and signal detection in climatic time series. Climatic change 33, 409–445.

Mendoza-Halliday, D., Major, A.J., Lee, N., Lichtenfeld, M.J., Carlson, B., Mitchell, B., Meng, P.D., Xiong, Y., Westerberg, J.A., Jia, X., 2024. A ubiquitous spectrolaminar motif of local field potential power across the primate cortex. Nature Neuroscience 1–14.

Miles, J.H., 2011. Estimation of signal coherence threshold and concealed spectral lines applied to detection of turbofan engine combustion noise. The Journal of the Acoustical Society of America 129, 3068–3081.

Mognon, A., Jovicich, J., Bruzzone, L., Buiatti, M., 2011. ADJUST: An automatic EEG artifact detector based on the joint use of spatial and temporal features. Psychophysiology 48, 229–240. https://doi.org/10.1111/j.1469-8986.2010.01061.x

Muralidharan, V., Aron, A.R., Cohen, M.X., Schmidt, R., 2023. Two modes of midfrontal theta suggest a role in conflict and error processing. NeuroImage 273, 120107. https://doi.org/10.1016/j.neuroimage.2023.120107

Muthukumaraswamy, S.D., 2010. Functional Properties of Human Primary Motor Cortex Gamma Oscillations. Journal of Neurophysiology 104, 2873–2885. https://doi.org/10.1152/jn.00607.2010

Myrov, V., Siebenhühner, F., Juvonen, J.J., Arnulfo, G., Palva, S., Palva, J.M., 2024. Rhythmicity of neuronal oscillations delineates their cortical and spectral architecture. Commun Biol 7, 1–18. https://doi.org/10.1038/s42003-024-06083-y

Navarro-Cebrian, A., Knight, R.T., Kayser, A.S., 2013. Error-Monitoring and Post-Error Compensations: Dissociation between Perceptual Failures and Motor Errors with and without Awareness. J. Neurosci. 33, 12375–12383. https://doi.org/10.1523/JNEUROSCI.0447-13.2013

Nelli, S., Itthipuripat, S., Srinivasan, R., Serences, J.T., 2017. Fluctuations in instantaneous frequency predict alpha amplitude during visual perception. Nat Commun 8, 2071. https://doi.org/10.1038/s41467-017-02176-x

Ostlund, B.D., Alperin, B.R., Drew, T., Karalunas, S.L., 2021. Behavioral and cognitive correlates of the aperiodic (1/f-like) exponent of the EEG power spectrum in adolescents with and without ADHD. Developmental Cognitive Neuroscience 48, 100931. https://doi.org/10.1016/j.dcn.2021.100931

Pascual-Marqui, R.D., Kochi, K., Kinoshita, T., 2024. Lagged coherence: explicit and testable definition. https://doi.org/10.48550/arXiv.2311.14356

Quinn, A.J., Lopes-dos-Santos, V., Dupret, D., Nobre, A.C., Woolrich, M.W., 2021a. EMD: Empirical Mode Decomposition and Hilbert-Huang Spectral Analyses in Python. Journal of open source software 6, 2977. https://doi.org/10.21105/joss.02977

Quinn, A.J., Lopes-dos-Santos, V., Huang, N., Liang, W.-K., Juan, C.-H., Yeh, J.-R., Nobre, A.C., Dupret, D., Woolrich, M.W., 2021b. Within-cycle instantaneous frequency profiles report oscillatory waveform dynamics. Journal of Neurophysiology 126, 1190–1208. https://doi.org/10.1152/jn.00201.2021

Rayson, H., Debnath, R., Alavizadeh, S., Fox, N., Ferrari, P.F., Bonaiuto, J.J., 2022. Detection and analysis of cortical beta bursts in developmental EEG data. Developmental Cognitive Neuroscience 54, 101069. https://doi.org/10.1016/j.dcn.2022.101069

Rayson, H., Szul, M.J., El-Khoueiry, P., Debnath, R., Gautier-Martins, M., Ferrari, P.F., Fox, N., Bonaiuto, J.J., 2023. Bursting with potential: How sensorimotor beta bursts develop from infancy to adulthood. J. Neurosci. https://doi.org/10.1523/JNEUROSCI.0886-23.2023

Schaworonkow, N., Voytek, B., 2021. Longitudinal changes in aperiodic and periodic activity in electrophysiological recordings in the first seven months of life. Developmental Cognitive Neuroscience 47, 100895. https://doi.org/10.1016/j.dcn.2020.100895

Sherman, M.A., Lee, S., Law, R., Haegens, S., Thorn, C.A., Hämäläinen, M.S., Moore, C.I., Jones, S.R., 2016. Neural mechanisms of transient neocortical beta rhythms: Converging evidence from humans, computational modeling, monkeys, and mice. Proceedings of the National Academy of Sciences of the United States of America 113, E4885-94. https://doi.org/10.1073/pnas.1604135113

Shin, H., Law, R., Tsutsui, S., Moore, C.I., Jones, S.R., 2017. The rate of transient beta frequency events predicts behavior across tasks and species. eLife 6. https://doi.org/10.7554/eLife.29086

Srinath, R., Ray, S., 2014. Effect of amplitude correlations on coherence in the local field potential. Journal of Neurophysiology 112, 741–751. https://doi.org/10.1152/jn.00851.2013

Szul, M.J., Papadopoulos, S., Alavizadeh, S., Daligaut, S., Schwartz, D., Mattout, J., Bonaiuto, J.J., 2023. Diverse beta burst waveform motifs characterize movement-related cortical dynamics. Progress in Neurobiology 228, 102490.

Taylor, J.A., Krakauer, J.W., Ivry, R.B., 2014. Explicit and implicit contributions to learning in a sensorimotor adaptation task. The Journal of neuroscience : the official journal of the Society for Neuroscience 34, 3023–32. https://doi.org/10.1523/JNEUROSCI.3619-13.2014

van Ede, F., Quinn, A.J., Woolrich, M.W., Nobre, A.C., 2018. Neural Oscillations: Sustained Rhythms or Transient Burst-Events? Trends in Neurosciences 41, 415–417. https://doi.org/10.1016/J.TINS.2018.04.004

Waschke, L., Donoghue, T., Fiedler, L., Smith, S., Garrett, D.D., Voytek, B., Obleser, J., 2021. Modality-specific tracking of attention and sensory statistics in the human electrophysiological spectral exponent. eLife 10, e70068. https://doi.org/10.7554/eLife.70068

Welch, P.D., 1967. The Use of Fast Fourier Transform for the Estimation of Power Spectra: A Method Based on Time Averaging Over Short, Modified Periodograms. IEEE Transactions on Audio and Electroacoustics 15, 70–73. https://doi.org/10.1109/TAU.1967.1161901

Wen, H., Liu, Z., 2016. Separating Fractal and Oscillatory Components in the Power Spectrum of Neurophysiological Signal. Brain Topogr 29, 13–26. https://doi.org/10.1007/s10548-015-0448-0

Yoo, K.H., Cannon, E.N., Thorpe, S.G., Fox, N.A., 2016. Desynchronization in EEG during perception of means-end actions and relations with infants' grasping skill. British Journal of Developmental Psychology 34, 24–37. https://doi.org/10.1111/bjdp.12115

Supplementary Figures

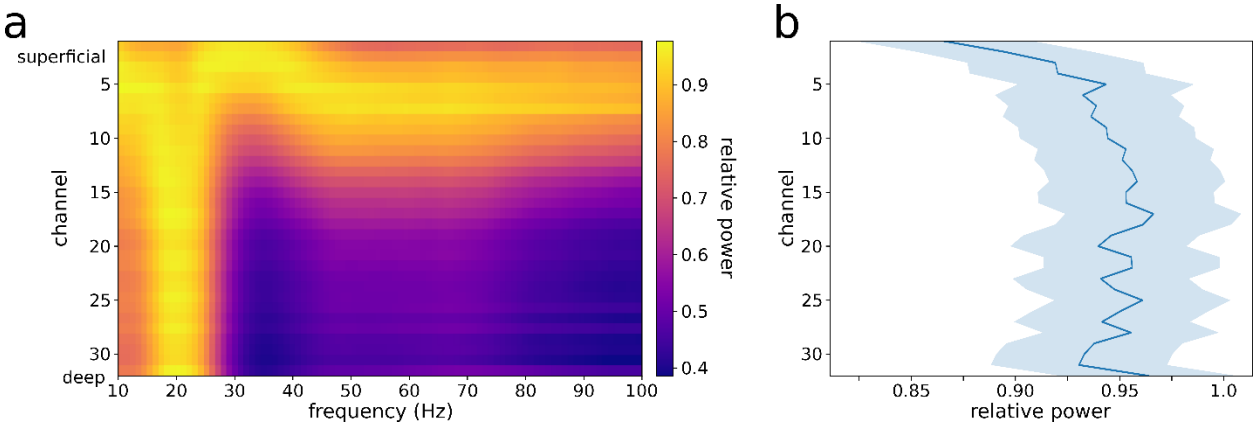

Figure S1. The relative power spectra (a) and relative beta power (b) of LFP data from the 32 channels averaged over all sessions from both monkeys.

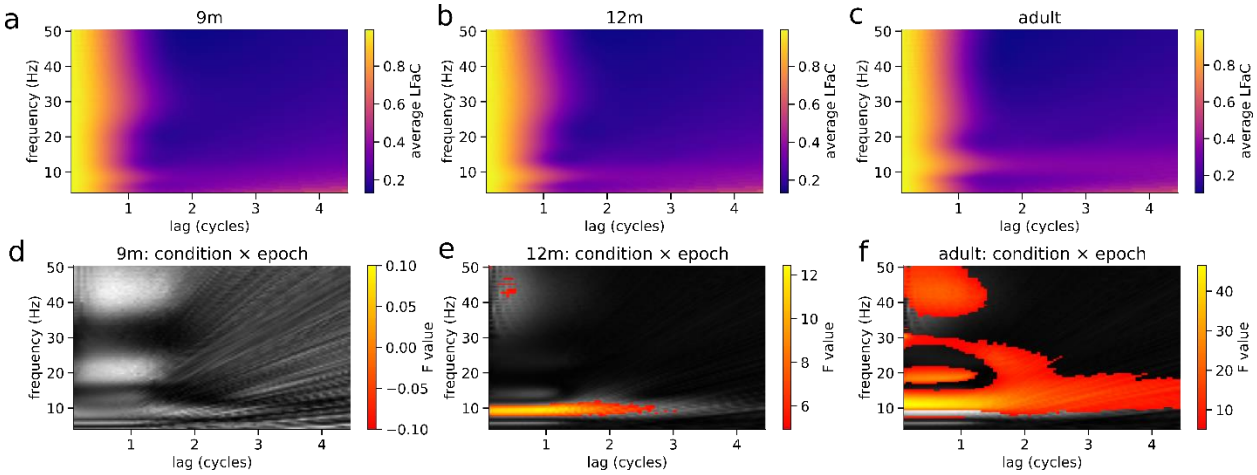

Figure S2. a-c) Group-averaged lagged Fourier autocoherence (LFaC) computed within EEG electrode clusters over sensorimotor cortex from 9-month, 12-month infants and adults. d-f) LFaC F statistics for the condition by epoch interaction for each group. Statistically significant clusters, corrected using cluster-based permutation tests, are shown in color.

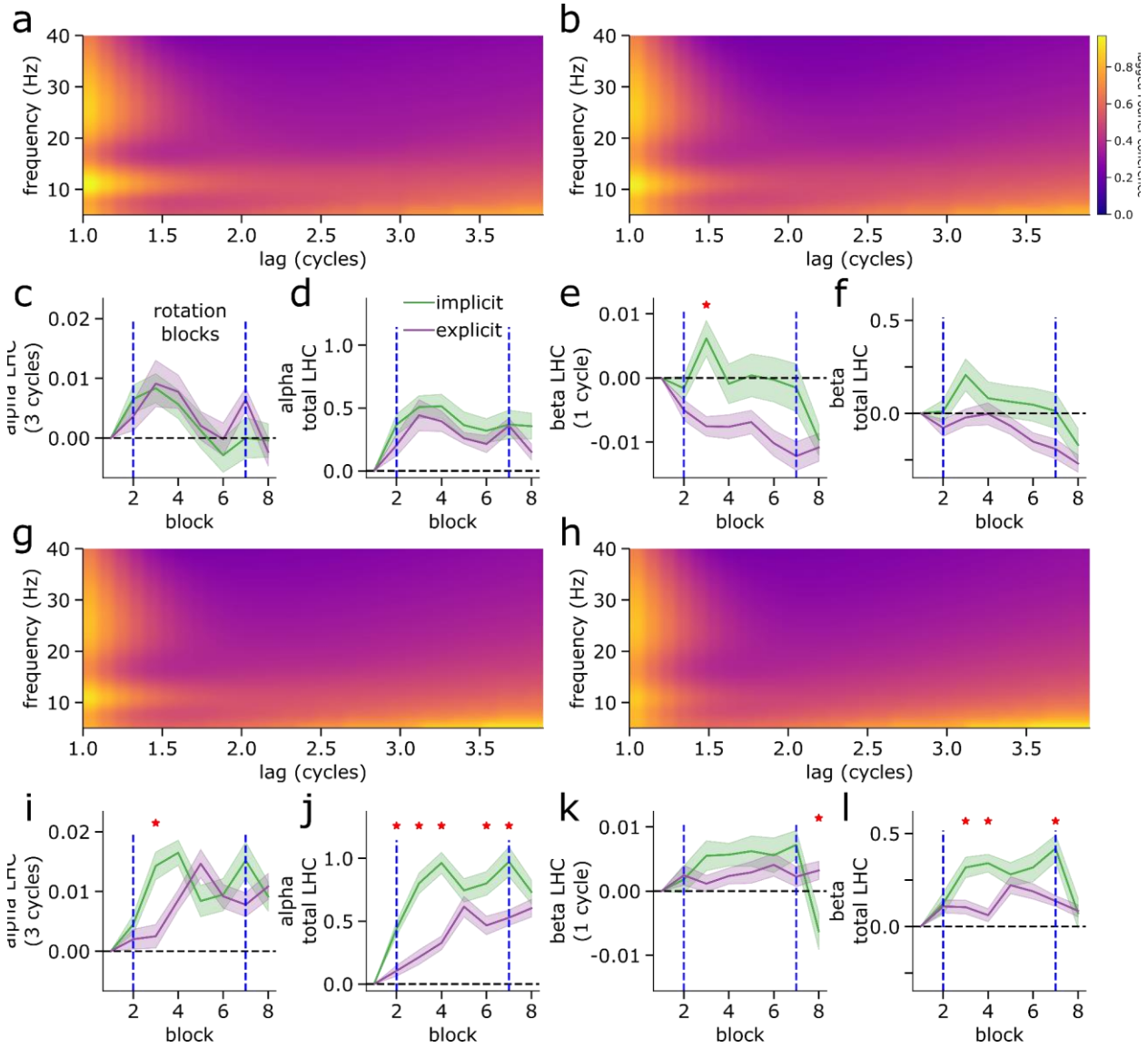

Figure S3. Alpha and beta lagged Fourier coherence during sensorimotor learning. a) Lagged Fourier coherence in left central sensors for the visual epoch in the implicit group, averaged over visuomotor rotation blocks. b) As in (a), for the explicit group. c) Alpha LFC at a lag of 3 cycles, for the visual epoch in each block. The solid lines indicate the mean value over subjects for the implicit (green) and explicit (purple) groups and the shaded areas represent the standard error. The vertical dashed lines indicate the beginning and end of the rotation blocks. d) As in (c), for the total alpha LFC. e) As in (c), for beta LFC at a lag of 1 cycle. Red stars indicate blocks in which LFC was significantly different between the two groups. f) As in (c), for the total beta LFC. g) Lagged Fourier coherence in left central sensors for the motor epoch in the implicit group, averaged over visuomotor rotation blocks. h) As in (g), for the explicit group. i) As in (c), for alpha LFC at a lag of 3 cycles in the motor epoch. j) As in (i), for the total alpha LFC. k) As in (i), for beta LFC at a lag of 1 cycle, l) As in (i), for the total beta LFC.

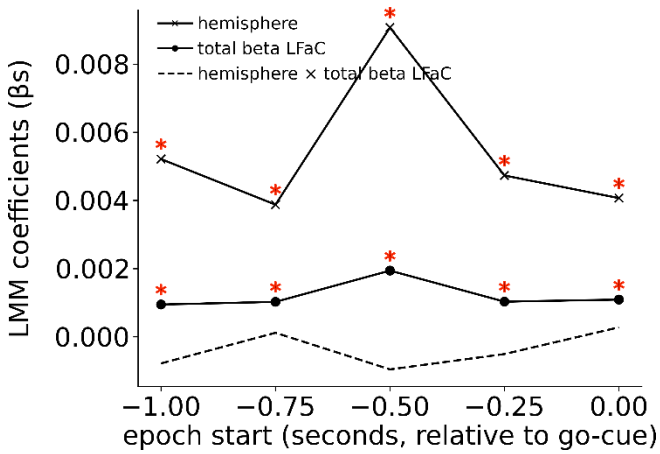

Figure S4. The estimated coefficients (βs) of linear mixed models fit to total beta LFaC computed in 1s epochs aligned from 1s, 0.75s, 0.5s, 0.25s, and 0s prior to the go cue. The significant effects are indicated with red stars.